Area-selective atomic layer deposition of noble metals: polymerized fluorocarbon layers as effective growth inhibitors

Petro Deminskyi,[*,†,‖] Ali Haider,[†] Hamit Eren,[§] Talha M. Khan,[†] and Necmi Biyikli[*,‡]

[†] UNAM-Institute of Materials Science and Nanotechnology, Bilkent University, Ankara 06800, Turkey

[‖] NASU-Institute of Microdevices, Technological & Analytical Research Department, Kyiv 04136, Ukraine

[§] Department of Chemical Engineering, Delft University of Technology, van der Maasweg 9, 2629 HZ Delft, The Netherlands

[‡] Electrical and Computer Engineering, University of Connecticut, 371 Fairfield Way, Storrs, CT, 06269-4157

Keywords: area-selective ALD, fluorocarbon, Pt, Pd, nucleation, growth inhibitor

ABSTRACT: The increasingly complex nanoscale three-dimensional (3D) and multi-layered structures utilized in nanoelectronic, catalytic, and energy conversion/storage devices, necessitating novel substrate-selective material deposition approaches featuring bottom-up and self-aligned precision processing. Here, we demonstrate the area-selective atomic layer deposition (AS-ALD) of two noble metals, Pt and Pd, by using plasma polymerized fluorocarbon layer as growth inhibition surfaces. Contact angle, X-ray photoelectron spectroscopy (XPS), and scanning electron microscopy (SEM) measurements were performed to investigate the blocking ability of polymerized fluorocarbon (CF_x) layers against ALD-grown metal films. Both Pt and Pd showed significant nucleation delays on fluorocarbon surfaces. Self-aligned film deposition is confirmed using this strategy by growing Pt and Pd on microscale lithographically patterned CF_x/Si samples. CF_x blocking layer degradation during ozone plasma exposure was analyzed using XPS measurments and results indicated it to be due to the oxygen physisorption with further hydroxyl groups formation on CF_x surface. Our work reveals that CF_x layers are compatible with ozone co-reactants up to the boundary condition when the blocking polymer can not withstand oxygen physisorbtion, and could potentially be used for radical-assisted AS-ALD processes for a wider selection of materials.

Atomic-scale precision manufacturing of next-generation complex three-dimensional (3D) device structures necessitates highly-selective bottom-up deposition strategies. As opposed to the conventional top-down approaches, area-selective deposition (ASD) provides self-aligned processing capability, which enhances the structural precision while reducing the overall fabrication complexity. The relatively recent efforts in area-selective atomic layer deposition (AS-ALD) unveiled the significant potential of ALD as a bottom-up materials synthesis technique which can be engineered towards achieving surface selectivity.[1-5] Being a surface-chemistry driven vapor synthesis method, ALD features iterative self-limiting growth cycles based on low-temperature ligand-exchange reactions.[6,7] The resulting deposition is highly controllable with sub-monolayer thickness accuracy, along with excellent 3D conformity and large-area uniformity.[8-14] The main target of AS-ALD efforts is to combine the unique features of ALD with surface selectivity, potentially leading to a versatile self-aligned fabrication tool-box.

Among others, area-deactivation approach became the main AS-ALD strategy, where self-assembled monolayers (SAMs) or various polymer films are utilized as growth blocking surfaces.[15,16] This way, selective deposition has been reported for oxides[4,17-19] (Al_2O_3, SiO_2, TiO_2, ZnO) and metals[20-23] (Pt, Pd, Ru, Rh, Ir, Co). Despite the promising results with various SAM chemistries, this approach suffered mainly from the difficulty in defect-free SAM synthesis, relatively long synthesis time, and CMOS-compatibility.[4,24-26] The latest reports by Bent *et* al. show that the time for SAM deposition reduced significantly with vapor-phase techniques instead of conventional liquid-phase synthesis, and yet provides sufficient blocking performance for conventional thermal AS-ALD processes.[1,27] However, both SAM and polymer blocking layers tend to degrade fairly quickly when radical-enhanced co-reactants are utilized including plasmas and ozone. This incompatibility with energetic co-reactants limits their use to merely thermal-ALD processes which excludes some critical materials.[28,29]

Platinum (Pt) and palladium (Pd) are amongst the most widely employed noble metals not only for CMOS logic and memory device fabrication,[30,31] but as well for catalysis,[32] energy conversion,[33] chemical sensing,[34,35] and energy storage.[36] Selective deposition of these noble metals is significantly needed for the fabrication of self-aligned metal-contact placement in 3D nanoscale device structures. Reports on AS-ALD of Pd are mostly related to the controlled synthesis of Pd/Pt core-shell nanoparticles using SAMs as blocking layers.[37] On the other hand, former efforts related to the AS-ALD of Pt include (i) electron-beam induced deposition,[38] which has compatibility issues for large areas and high-aspect-ratio structures, (ii) use of PMMA and polyimide (PI) blocking layers for thermal Pt-ALD which degrade under radical/plasma exposure,[39] and (iii) topographically selective Pt-ALD on the vertical sidewalls of fin structures via ion-implanted ultrathin fluorocarbon films as growth inhibition horizontal surfaces.[2] Selective noble-metal ALD featuring energetic co-reactants such as ozone are yet missing. Growth inhibitors needed for such energetic ALD processes should ideally exhibit sufficient radical-resistance, a defect/pinhole-free microstructure, CMOS-compatibility, ease of deposition, and thermal stability.[15]

Our previous work on AS-ALD of metal-oxide films where we used inductively coupled plasma (ICP)-polymerized fluorocarbon (CF_x) coatings as blocking layers, showed effective ZnO growth inhibition with self-aligned patterning and no growth blocking capability for TiO_2.[40,41] Utilization of a CMOS-standard plasma-polymerized CF_x film along with its relative ease of control, revealed this approach with significant potential. In this work, we demonstrate that polymerized fluorocarbon surfaces can function as effective growth inhibitors for ALD-grown Pt and Pd films as well. Besides providing successful growth blocking for Pt and Pd, ozone-assisted Pt ALD experiments revealed that polymerized CF_x layers are also ozone-compatible. To the best of our knowledge, this is the first demonstration of an AS-ALD process utilizing ozone as co-reactant for noble metals. When compared to the ion-implanted ultra-thin CF_x blocking layers,[2] our approach provides a complementary CMOS-compatible solution to inhibit Pt and Pd deposition on non-horizontal surfaces of 3D nanostructures. This strategy might pave the way for the selective deposition of alternative materials which necessitate energetic co-reactants.

Film growth: CF_x layer was deposited in a commercial ICP etch reactor (SPTS MPX-ICP), conventionally used for deep reactive ion etching (DRIE) process of Si wafers. Deposition of ~60 nm of CF_x was performed for ~70 sec using C_4F_8 (99.998% purity, Linde) gas flow rate of 70 sccm, under 400 W radio frequency plasma power at 13.56 MHz. Si (100) reference control samples were solvent cleaned (acetone, isopropyl alcohol, de-ionized water rinse, and N_2 blow dry) and exposed to O_2 plasma in an asher system (100W, 50 sccm) for 2 minutes before ALD of Pd in order to increase the concentration of hydroxyl groups on the substrate which should eliminate any possible nucleation delays on Si surface.[40] The reference control samples for Pt study were not pre-treated in O_2 plasma before the main Pt ALD growth due to the ozone-based plasma process that increasing the hydroxyl groups on the substrate within the process. Pt and Pd deposition on bare and CF_x-coated Si (100) samples was accomplished by using trimethyl (methylcyclopentadienyl) platinum(IV) ($MeCpPtMe_3$) and palladium(II) hexafluoroacetylacetonate ($Pd(hfac)_2$) as metal precursors. Ozone (O_3) and formalin (CH_2O) were utilized as co-reactants for Pt and Pd growth, respectively. ALD experiments with different cycle numbers were carried out at 150°C and 200°C for Pt and Pd respectively, using a Savannah S100 ALD reactor, (Veeco/CambridgeNanotech Inc.) using N_2 as the carrier and purge gas. One unit growth cycle of Pt consisted of $MeCpPtMe_3$ pulse (0.2 s), N_2 purge (15 s), ozone pulse (0.1 s), and N_2 purge (15 s). $MeCpPtMe_3$ precursor was preheated to 65°C and stabilized at this temperature prior to ALD cycles. One growth cycle of Pd consisted of $Pd(hfac)_2$ pulse (0.4 s), N_2 purge (10 s), formalin pulse (0.15 s), and N_2 purge (10 s). $Pd(hfac)_2$ precursor was preheated to 70°C and stabilized at this temperature prior to deposition experiments. Formalin was kept at room temperature during the growth. Total stabilization time before growth both for Pt and Pd was ~20 min.

Film characterization and patterning: Contact angle of bare and CF_x-coated Si (100) substrates have been measured before and after ALD growth cycles, using static contact angle measurement setup (OCA 30). A 4 µL-water droplet was dropped on the sample surfaces to measure the contact angle. Film thicknesses of CF_x have been determined using a variable angle spectroscopic ellipsometer (V-VASE, J.A. Woollam Co. Inc., Lincoln, NE) which is coupled with a rotating analyzer and xenon light source. The ellipsometric spectra were collected at three angles of incidence (65°, 70°, and 75°) to yield adequate sensitivity over the full spectral range. Film thickness values were extracted by fitting the spectroscopic ellipsometer data using Cauchy model, while substrate was taken as default Si (100) in V-Vase Woollam software. Elemental composition and chemical bonding states of the metallic thin films were obtained by XPS measurements using Thermo Scientific K-Alpha spectrometer (Thermo Fisher Scientific) with a monochromatized Al Kα X-ray source (spot size ~400 µm). All peaks in XPS survey scans are referenced to C 1s peak for charge correction and quantification of survey scans have been performed using Avantage software. Surface morphologies of Pt and Pd-coated samples were determined using high-resolution FIB-SEM system (FEI, Nova 600i Nanolab) and the cluster size were determined using "Image J" software. In order to pattern CF_x via lithography on Si (100) substrates, ~1.4 µm of AZ5214 photoresist (Microchemicals GmbH) is spun on the wafer and is patterned into a checkerboard and parallel striped lines using a suitable photomask and photolithography. The wafer is then hard baked at 110°C for 5 min, followed by the ICP-polymerization process in the ICP reactor. Once the deposition is complete, the wafer is soaked into acetone for lift-off process of the CF_x layer portions on top of the patterned photoresist. The resulting wafer with patterned CF_x layer is solvent-cleaned before subsequent metal-ALD growth experiments. XPS line-scan was performed on the resulting Pt and Pd-coated samples to determine the selectivity performance as a function of ALD cycles, using the same XPS system with a spot size of ~100 µm, scanning step size – 41 µm and 43 µm, and number of scanning points – 100 and 176 for Pt and Pd, respectively. The selectivity values for Pt and Pd as a function of ALD cycles were determined from Equation 1 (based on XPS elemental concentrations of Pt or Pd on CF_x and Pt or Pd on Si):

$$\text{Selectivity} = \frac{A_{Si} - B_{CFx}}{A_{Si}}, \qquad (1)$$

where A_{Si} and B_{CFx} – are the atomic % of ALD deposited material on Si or CF_x surfaces respectively. Taking into account that amount of deposited material on the passivated surface is usually below the detection limit of XPS, SEM; Blocking polymer surface reactions with precursors appeared after the initial ALD cycles but it stays below the detection limit for considerable time, through the whole paper we assume that the nucleation delay corresponds to the detectable nucleation delay.

(i) Pt nucleation and selectivity. In the first part of our selective deposition study, Pt film nucleation and growth behavior on CF_x and Si surfaces via ozone-based low-temperature ALD is explored. Initial contact angles of Si and CF_x/Si samples before the ALD cycles were measured as ~71° and ~114°, respectively. After the initial 50 ALD cycles, the contact angles on the same samples were measured as 77.4° and 106.4°, respectively, marking an increase for Si and decrease for CF_x surfaces. The contact angle on Si (100) decreased to ~67.4° after 250 Pt-ALD cycles, while it remained almost unchanged for CF_x coated sample with a relatively narrow fluctuation between ~104° and 106° up to 250 cycles (Figure 1a). Subsequently, we analyzed the evolution of Pt nucleation by measuring the Pt-island/cluster size on Si and CF_x samples as a function of ALD cycles. Figure 1b shows how the average Pt cluster size evolved on both sample surfaces with increasing the number of ALD cycles, which clearly indicates a considerable nucleation delay on CF_x surface. While no Pt clusters were detected up to 150 cycles, ~2 nm and ~5 nm Pt cluster were observed on CF_x samples after 200 and 250 ALD cycles, respectively, with relatively

low density and surface coverage with respect to Si (100) reference samples. On the other hand, Pt nucleated easily on Si (100) surface exhibiting ~3 nm sized Pt clusters with high density after 50 ALD cycles which increased and saturated up to ~15 nm for 200 and higher cycle numbers.

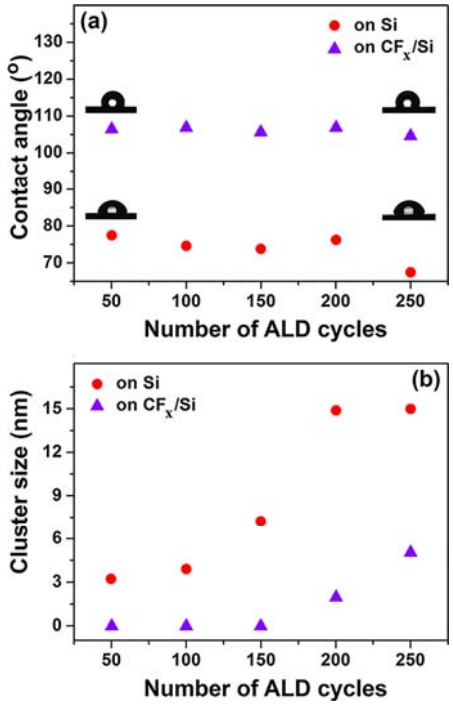

Figure 1. Variation in (a) contact angle and (b) average Pt cluster size as a function of ALD growth cycles on fluorocarbon coated and bare Si (100) substrates. Despite a relatively constant contact angle, fluorocarbon surface shows Pt-nucleation inhibition character for more than 150 ALD cycles.

Figure 2a–e and Figure 2f–j show the obtained images from the Si (100) and CF_x sample surfaces after 50, 100, 150, 200, and 250 ALD cycles, respectively. The initial 50 cycle results clearly reveals successful Pt nucleation on Si (100) with increase in both Pt nanoparticle (NP) density and cluster size leading towards coalescence into larger islands (~15 nm for 200+ cycles) and eventually complete surface coverage as continuous Pt film. However, in contrast to the bare Si (100) sample, CF_x/Si sample surface is free from any detectable Pt nucleation after 150 cycles. Platinum nucleation on CF_x becomes evident only after 200 ALD cycles with initial average Pt-cluster diameter of ~2 nm and relatively non-uniform surface distribution. As a result, the initial Pt NP seeds on CF_x surface function as growth centers during the further ALD cycles featuring half-cycle exposures of $C_9H_{16}Pt$ and ozone. The average Pt cluster size increases to ~5 nm at 250 cycles which signs the considerable modification of CF_x surface, not being able to block the rapid Pt-nucleation after 200 ALD cycles.

Table 1 summarizes how the platinum and oxygen content from the surface of CF_x/Si and Si (100) samples evolve during ALD cycles via XPS survey scans. Other than Pt and oxygen content – more detailed information related to the elemental composition of Si, C, and F are presented in Table S1. XPS measurements of the CF_x sample surface show the absence of a detectable Pt signal for 50 and 100 ALD cycles. After 150 ALD cycles, a very weak Pt signal is detected, corresponding to only ~0.01 at. % which increased an order of magnitude – but still relatively low (~0.07 at. %) for 200 ALD cycles. Further increase in Pt-ALD cycles up to 250 cycles indicates a stronger increase of Pt content to ~2.6 at.%, confirming the practical Pt-nucleation onset for ALD cycles higher than 200.

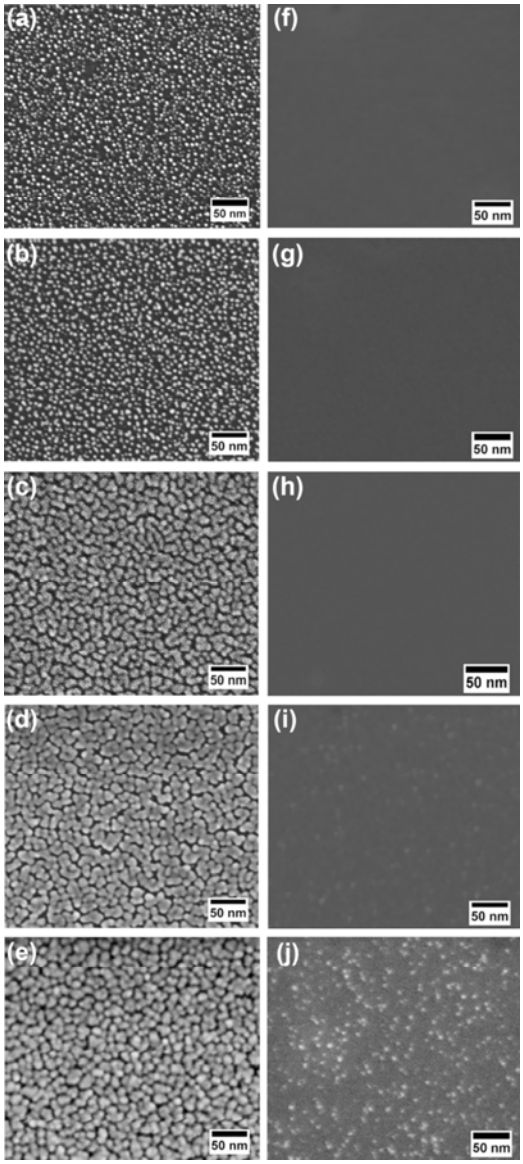

Figure 2. SEM images of (a-e) bare Si (100) and (f-j) CF_x/Si (100) sample surfaces at various stages in Pt-ALD growth experiments (a, f) 50 cycles; (b, g) 100 cycles; (c, h) 150 cycles; (d, i) 200 cycles; and (e, j) 250 cycles.

The combination of the adsorption of the noble metal precursor and the use of reactive ozone starts to show its effect on ICP-polymerized CF_x layer only after 250 ALD growth cycles. XPS measurements of the CF_x coated sample exposed to 250 Pt-ALD cycles show oxygen content fluctuating within ~2–4 at. % which confirms the relative stability of ICP-polymerized CF_x surface against degradation during reactive ozone exposure till the formation of hydroxyl groups (that behave like nucleation centers for Pt growth) and Pt on the surface. To the best of our knowledge, this result represents the first demonstration of a selective ALD process featuring reactive ozone as co-reactant for platinum deposition.

Table 1. Variation in Pt and O at. % on CF_x/Si samples and selectivity value as a function of ALD cycles.

Number of ALD cycles	on CF_x/Si		Pt/CF_x to Pt/Si selectivity
	Pt at. %	O at. %	
50	–	1.03	~1
100	0.01	1.57	
150	0.01	1.81	
200	0.1	2.17	~0.99
250	2.62	4.44	~0.95

Figure 3a shows the XPS survey scan results obtained for CF_x/Si samples recorded at 50, 100, 150, 200, and 250 ALD cycles. While detecting C 1s, O 1s, and F 1s peaks from CF_x surface, absence of Pt 4f peak confirms the successful Pt-nucleation inhibition for more than 150 ALD cycles. These results demonstrating the effective nucleation inhibition behavior of ICP-polymerized CF_x films as highly effective growth blocking surfaces. Moreover, the XPS survey scan results provide excellent correlation with SEM observations as well as contact angle measurements and cumulatively approve that CF_x inhibits Pt deposition for ~200 growth cycles, which is equivalent to a growth blocking thickness of ~17 nm. It corresponds to the selectivity of ~0.99 while for 250 cycles a selectivity drops to ~0.95.

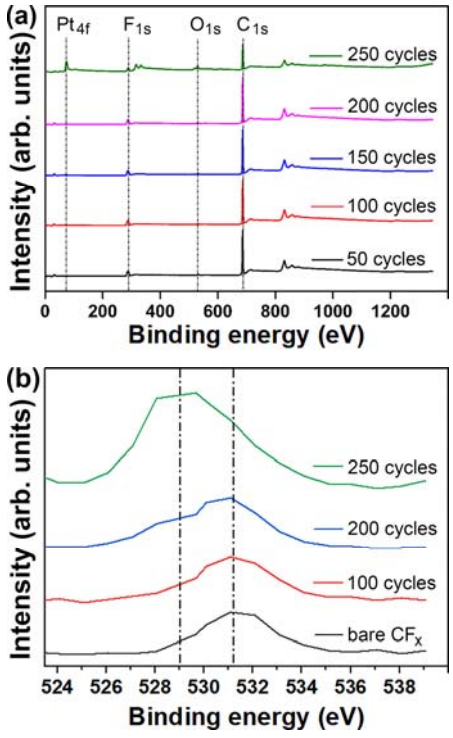

Figure 3. (a) XPS survey scans of CF_x/Si (100) sample after 50, 100, 150, 200, and 250 Pt-ALD cycles, with a nearly 200-cycle nucleation delay is observed on polymerized CF_x surface, and (b) XPS scans of O 1s obtained on bare CF_x, and CF_x/Si (100) after 100, 200, and 250 Pt-ALD cycles.

An in-depth study on the reaction-resistance of the fluorocarbon layer with ozone-based process represented by the investigation of the O 1s peaks on the CF_x/Si substrate before and after deposition of 100, 200, and 250 of Pt ALD cycles from the XPS scan (Figure 3b). O 1s is detected on the CF_x substrate before and after Pt growth, with the O 1s peak located at 531.08 eV (I) corresponds to hydroxyl groups (OH) on the surface of CF_x that is in good agreement with hydroxide signal (531.5 ±0.5 eV) that is a typical value for binding energies for oxides.[42] We also note another interesting observation: on CF_x layer, the O1s peak is broadening to the lower binding energies with the peak intensity at 529.68 eV (II) for 250 cycles of Pt ALD that could be assigned to the oxygen atoms directly bound to metallic Pt.[43,44] The mechanism of the Pt nucleation on CF_x is currently not fully understood. Our key hypothesis is that, during the ozone half-reaction, oxygen slowly physisorbed into the CF_x film. This diffusion is likely enhanced during additional ozone plasma exposure. In the same time during the $MeCpPtMe_3$ half-reaction, hydroxyl groups form on the centers of oxygen vacancies that create the preferable centers for further Pt growth. Although the hydroxyl groups are created on CF_x surface, the amount of Pt that could be chemisorbed on such active sites still is under the detectable limit of XPS up to 150 cycles.

Figure 4 shows Pt 4f HR-XPS scans measured on CF_x/Si samples. HR-XPS scans taken after 50, 100, 150, 200, and 250 cycles of Pt-ALD. XPS measurements of CF_x coated Si samples after 50, 100, 150, 200, and 250 cycles of Pt-ALD show no considerable Pt signal up to 200 cycles (Figure 4b and Table S3). At 200 and 250 cycles, we observe the signals at 77.19 eV and 76.76 eV belonging to Pt 4f peaks. Pt 4f peak for 200 growth cycles can be deconvoluted into two sub-peaks centered at 75.40 eV and 78.56 eV, which are assigned to be PtOH and platinum (IV) oxide state (PtO_2), respectively. Pt 4f peak for 250 growth cycles, on the other hand, can be deconvoluted into two sub-peaks centered at 74.91 eV and 78.29 eV, which are assigned to be metallic Pt and platinum (IV) oxide state (PtO_2), respectively. After XPS data fitting, we deconvoluted Pt 4f peak for 200 growth cycles into two main separate subpeaks (Figure 4b) centered at 75.40 eV (subpeak A) and 78.56 eV (subpeak B), which are assigned to be PtOH and platinum (IV) oxide state (PtO_2), respectively. In the same manner, we deconvoluted Pt 4f peak for 250 growth cycles (Figure 4c) into two individual peaks centered at 74.91 eV (subpeak A) and 78.29 eV (subpeak B), which are assigned to be metallic Pt and platinum (IV) oxide state (PtO_2), respectively. Additional information related to the Pt HR-XPS scans measured on Si samples are represented in Supporting information. This result is also in good agreement with the trend observed in Si (100) reference samples where dominantly oxide states in the initial 50-100 cycles were transformed to metallic states at higher ALD cycle numbers. The HR-XPS scans of Pt 4f on Si (100) are provided in Figure S1.

Another important observation was the thickness stability (~60 nm) of CF_x blocking layer regardless of the Pt ALD cycles which featured reactive ozone exposures. Absence of any decrease in CF_x thickness under ozone cycles might be attributed to the relatively strong C-F bonding which prevented any film etching reaction during excessively long ozone exposure at temperatures up to 150°C. In addition to the inherent unreactive nature of CF_x, stability in thickness of CF_x reminds potential for further investigation of AS-ALD under alternative energetic co-reactants and plasma chemistries in radical-assisted ALD processes.

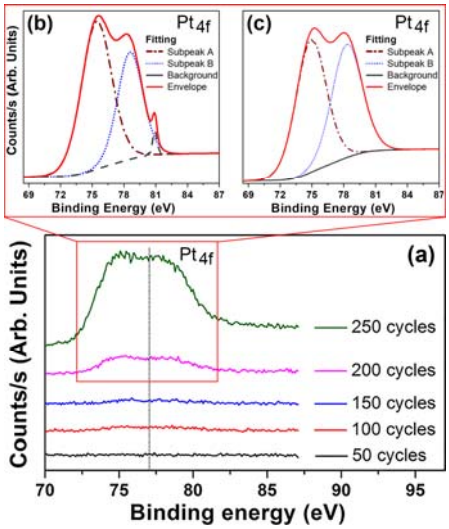

Figure 4. HR-XPS survey scans of Pt 4f obtained on (a) CF_x/Si (100) after 50, 100, 150, 200, and 250 Pt-ALD cycles together with HR Pt peaks after 200, 250 cycles (b, c) and additional fitting.

(ii) Selective Pt deposition and self-aligned patterning. Selective Pt deposition on lithographically patterned CF_x/Si samples was studied with 180 Pt-ALD cycles using EDX and XPS line scan measurements and HR-SEM imaging as shown in Figure 6a-c. XPS line scan was performed on mm-scale Pt patterns (Figure 6a) where Pt 4f intensity was measured (Figure 6b). Pt 4f peak is only observed in bright-looking regions where CF_x layer was lifted-off, while CF_x regions with dark color contrast exhibit Pt 4f intensity as background (noise-floor) signal, confirming the absence of Pt deposition on CF_x surface. The reason of a gradual increase in Pt 4f intensity going from CF_x surface to Pt could be attributed to the spot size of the monochromatized Al Kα X-ray source that was set to ~100 µm during the XPS line-scan, value of scanning steps and a number of scanning points. At the CF_x/Pt interface, due to the relatively large XPS spot size, we simultaneously detect signals from both CF_x and Pt covered surfaces which causes a gradual increase in the observed Pt intensity. The uniform blocking of Pt growth on the CF_x pattern was confirmed by the HR-SEM image which depicts a sharp CF_x/Pt interface (see Figure 6a). Figure 6c shows the EDX line-scan measurement, revealing Pt M X-ray quanta being detected along the scan-line. As expected, the intensity of Pt M X-ray quanta increases only in line-patterns where CF_x was lifted-off, which reaffirms the self-aligned patterning of Pt line structures at micro-scale.

EDX elemental mapping images are shown in Figure 7, which are performed to indicate the coverage and distribution of platinum, carbon, and fluorine elements on the patterned CF_x/Si sample surface. Figure 7a corresponds to SEM image of patterned Pt line features through which elemental maps of Pt, C and F are collected. Figure 7b-d show elemental maps of C K, Pt M, and F K, respectively. These results confirm both successful patterning of CF_x and area-deactivated AS-ALD deposition of Pt up to at least 180 ALD cycles. We have used 180 cycles of Pt-ALD to avoid any possible nucleation which appeared after 200 growth cycles and to show optimal conditions for maximum possible Pt nucleation on Si while CF_x surface still shows near-ideal Pt-nucleation inhibition.

(iii) Pd nucleation and selectivity. The Pd-ALD growth experiments using $Pd(hfac)_2$ and formaline precursors were carried out on CF_x-coated and uncoated Si (100) substrates for 200, 400, 600, 800, 1000, 1500, and 2000 ALD cycles. Figure 8a, b depicts the variation in the measured contact angle and average Pd-cluster size of the exposed substrates with an increasing number of ALD cycles. At the end of the first 200 Pd-ALD cycles, the contact angle of Si sample decreased from ~71° to ~57°, while CF_x-coated sample exhibited only a slight decrease from ~114° to ~110°. With further increase in ALD-cycles up to 2000 cycles on Si (100) samples, contact angle exhibited an increase and fluctuated between ~68–72°. The increasing of the contact angle with increasing of the number of ALD-cycles (Figure 8a) can be attributed to the topography (the impact of the surface roughness due to the changes in palladium nanoparticles dimensions (Figure 8b).[45,46] In contrast, CF_x samples exhibited rather a stable contact angle values around ~109°, almost independent from the number of ALD cycles up to 1000 cycles. However, the contact angle decreased to ~95° for Pd growth cycles higher than 1500, signaling a possible nucleation onset for Pd film growth on CF_x surface.

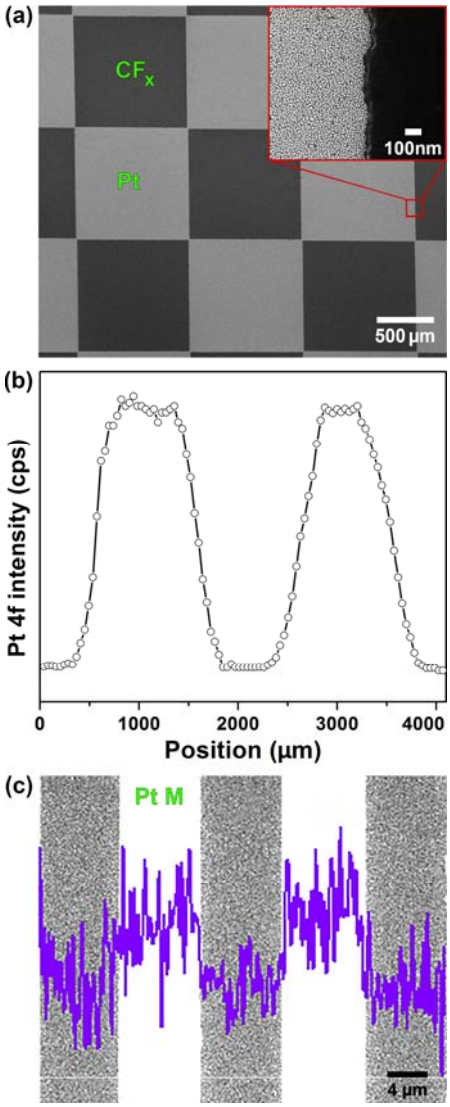

Figure 6. (a) SEM image and (b) XPS Pt 4f line scan obtained from Pt-ALD grown on mm-scale patterned CF_x/Si (100) sample. (c) EDX Pt M line scan superposed on the SEM image obtained from µm-scale CF_x/Si (100) patterned sample after 180 Pt-ALD cycles.

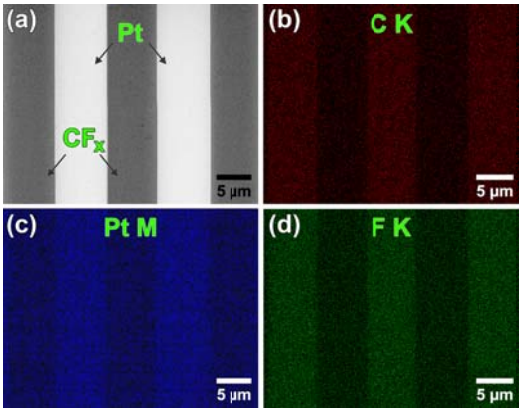

Figure 7. SEM image of (a) Pt/CF_x patterned sample after 180-cycle ALD experiment. Elemental mapping of (b) C K, (c) Pt M, and (d) F K signals. Pt is colored in blue, while red and green show C and F elements, respectively.

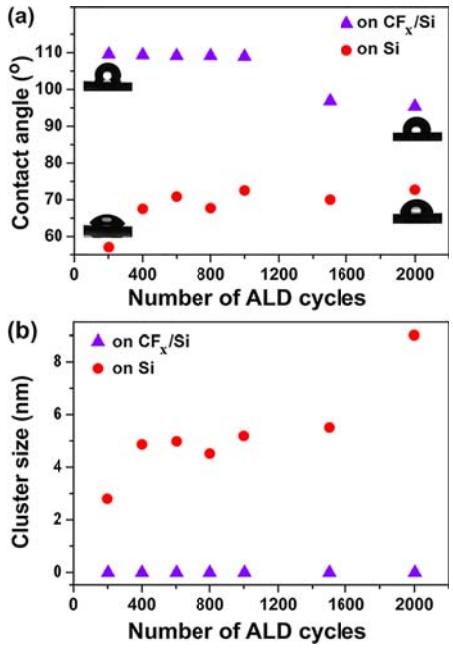

Figure 8. Variation in (a) contact angle and (b) average Pd-cluster size with number of ALD cycles on CF_X/Si and bare Si (100) samples.

These results indicate that plasma polymerized CF_x layer retains its rather hydrophobic and inert character up to more than 1000 Pd-ALD cycles while its surface state starts to show an initial change around 1500 cycles. Subsequently, SEM measurements were performed to visualize the nucleation and cluster-growth behavior of Pd on CF_x-coated and bare Si (100) sample surfaces. Figure 10a–e and Figure 10f–j are representative HR-SEM images of Pd ALD on bare and CF_x-coated Si (100) samples after 200, 600, 1000, 1500, and 2000 ALD cycles, respectively. In agreement with the contact angle measurements, SEM images show apparently no measurable evidence of Pd growth on CF_x surface up to the maximum 2000 ALD cycles we have studied. This is in strong contrast to Pd nucleation and growth behavior on Si (100), where Pd nucleates right away and Pd NPs are apparent after the initial 200 ALD cycles. Further increase in Pd growth cycles on Si (100) leads to an increase in density and size of Pd-NPs, eventually coalescing into larger and densely packed Pd islands, with an estimated effective film thickness of ~10 nm that corresponds to a selectivity of ~0.99.

On the other hand, polymerized CF_x film retained its inhibiting character till the maximum number (2000) of growth cycles tested. Literature reports indicate that organic blocking layers used for selective ALD, exhibit degradation beyond some upper limit of ALD growth cycles, eventually resulting in unwanted nucleation and failure to block film growth. This result has in part been attributed to cumulatively long exposures of the organic blocking layers to relatively high substrate temperatures. Although CF_x layer showed significant inhibition against Pd growth up to 2000 ALD cycles (a total exposure to 200°C for ~12 hours), as will be confirmed with XPS results, this does not imply that CF_x will not fail eventually beyond a certain number of ALD cycles. These results are achieved without a detailed and systematic recipe optimization for Pd growth since the main aim of this study was to explore the noble-metal nucleation inhibition properties of the polymerized CF_x layers. As a follow-up study, the ALD growth conditions might be further adjusted to achieve enhanced selectivity and shortened growth durations.

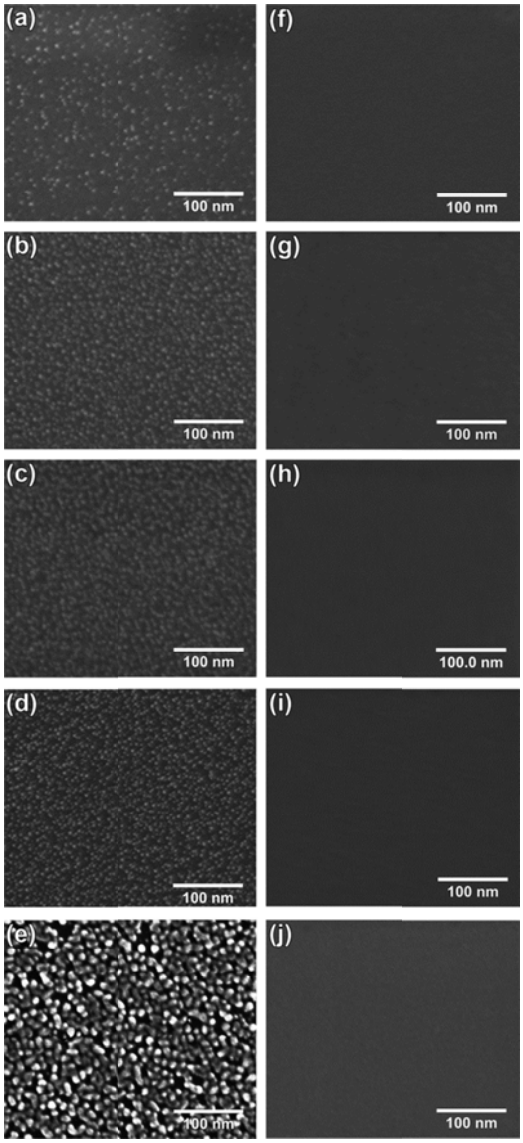

Figure 10. SEM images of the substrate surfaces of (a-e) bare Si (100) samples and (f-j) CF_x-coated samples obtained at various stages of the Pd-ALD experiment: (a, f) 200 cycles (b, g) 600 cycles (c, h) 1000 cycles (d, i) 1500 cycles, and (e, j) 2000 cycles.

Table 2 summarizes the quantification of Pd content (at. %) from XPS survey scans for Pd on CF_x/Si and bare Si (100) substrates. Other than Pd content – more detailed information related to the elemental composition of Si, C, O, F are presented in Table S4. The amount of Pd on CF_x/Si samples was calculated as ~0.02 % using XPS data, regardless of the number of ALD cycles up to 1500 cycles. This result again confirms that CF_x is efficiently blocking Pd nucleation for at least 1500 ALD cycles. With an additional 500 cycles, the 2000-cycle Pd-ALD sample on CF_x/Si substrate indicates a slight but yet observable increase to ~0.12 %. Despite the fact that this atomic percentage corresponds to typically less than a monolayer of Pd deposition, we can safely claim that the complete Pd-nucleation blocking property of ICP-polymerized CF_x is degraded after 2000 cycles of Pd-ALD. Pd content on bare Si (100) substrate samples, on the other hand, show a strongly correlated increase with number of ALD growth cycles, confirming the absence of Pd nucleation inhibition of Si surfaces.

Table 2. Variation in Pd at. % on CF_x/Si samples and selectivity value as a function of ALD cycles.

Number of ALD cycles	Pd at. % on CF_x/Si	Pd/CF_x to Pd/Si
200	0.02	~1
400	0.03	
600	0.03	
800	0.03	
1000	0.02	
1500	0.03	
2000	0.12	~0.99

XPS data from both Si and CF_x samples were recorded at various growth stages to determine the surface elemental composition as well as the chemical bonding states (see Figure 11). C 1s, O 1s, and F 1s peaks were detected from CF_x surface irrespective of the number of Pd-ALD cycles. Absence of the Pd 3d peak corroborate the previous findings that CF_x successfully inhibits Pd nucleation while Pd growth on Si (100) surface reveals the peak of Pd 3d right after the first 200 ALD cycles.

To further analyze and confirm Pd nucleation inhibition on CF_x surface, Pd_{3d} high-resolution XPS (HR-XPS) scans were carried out and the resulting peak spectra measured on Si (100) and CF_x/Si as a function of total ALD cycles are shown in Fig. 10. All recorded peaks were fit after a charge-correction with respect to the adventitious C 1s spectra component (C-C, C-H) with binding energy set to 284.8 eV. HR-XPS spectra exhibits Pd $3d_{5/2}$ and Pd $3d_{3/2}$ spin-orbit doublet peaks for the ALD-grown Pd on Si substrates. The detected bonding species, their corresponding spectral lines, and binding energy values for the grown Pd film have been summarized in Table S5. For the initial 200 and 400 growth cycles, Pd-O and Pd-O_x bonding scheme have also been detected in addition to the main Pd-Pd core level bonding. Figure 12a shows that beyond 400 growth cycles, Pd $3d_{5/2}$ and Pd $3d_{3/2}$ peaks corresponding only to Pd-Pd bonding interactions have been detected, confirming the formation of small Pd clusters leading to larger Pd agglomerations and eventually Pd thin films.[47,48] On the contrary, no detectable Pd signal is observed in the HR-XPS data obtained from CF_x/Si (100) samples inferring near-ideal Pd-nucleation inhibition on CF_x up to 2000 ALD cycles.

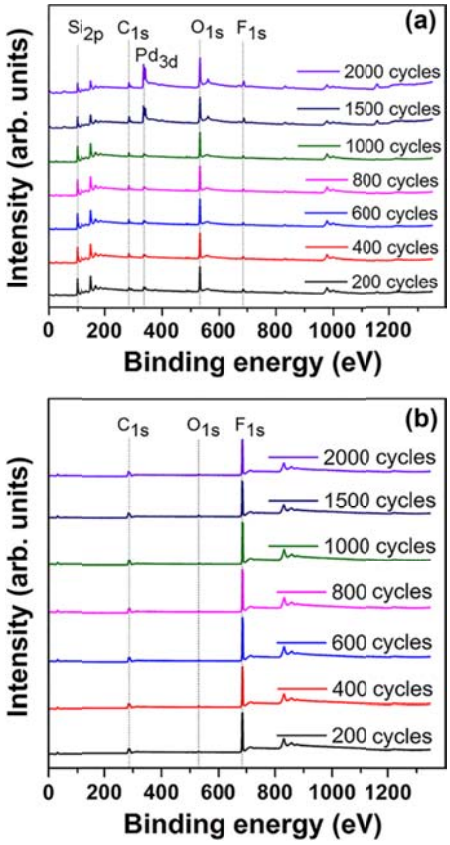

Figure 11. XPS survey scans of (a) Si (100) and (b) CF_x/Si samples at various stages of Pd-ALD growth experiments, which confirmed effective Pd-nucleation blocking of CF_x surface up to 2000 Pd-ALD cycles.

(iv) Selective Pd deposition and self-aligned patterning. Similar to our Pt studies, we carried out self-aligned film patterning experiments via selective Pd deposition on lithographically patterned CF_x/Si substrates. Positive CF_x patterns were formed for the analysis and visualization of possible edge effects in selective Pd-growth on Si (100) and growth inhibition on CF_x, respectively. Pd deposition was carried out for 2000 ALD cycles on patterned CF_x/Si samples which are subsequently characterized by SEM, EDX line scan, EDX elemental mapping, and XPS line scan measurements. Figure 13a, b show SEM images of the Pd patterns which legibly indicate the selective deposition of Pd metal (brighter regions) along with with clear and uncoated CF_x surface (darker circular spots). HR-SEM image from the Pd/CF_x interface shows no Pd deposition signs on top of polymerized CF_x patterns except a narrow transition region (50–100 nm) corresponding to the width of the lifted-off CF_x layer sidewall. Within these transition areas, Pd nanoparticles with smaller cluster size and lower density are observed due to the imperfections of the conventional photolithographic patterning process.

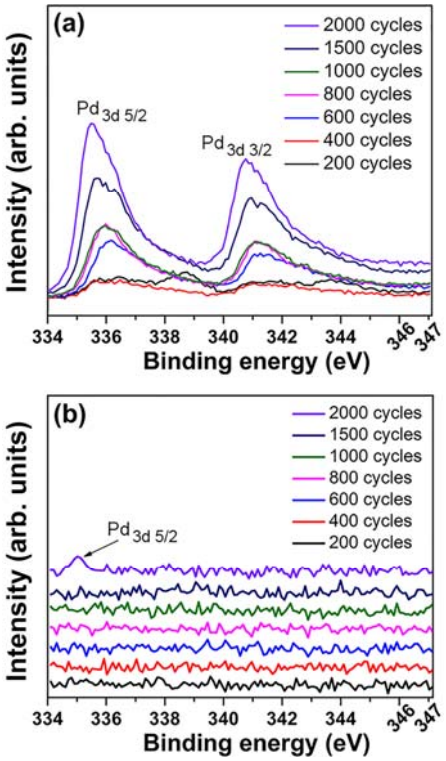

Figure 12. HR-XPS survey scans of Pd 3d obtained at different stages of Pd-ALD on (a) Si (100) and (b) CF_x/Si (100), confirming the near-ideal complete inhibition of Pd deposition on CF_x surface.

To analyze the elemental composition variation along the Pd/CF_x patterns, EDX and XPS line scan was performed, depicted in Figure 14. XPS line scan was performed on larger mm-scale Pd patterns (Figure 14a) as the survey spectra for this measurement were recorded with an X-ray beam size of 400 µm, along with ~50 µm steps between each data point. Pd 3d intensity was measured in terms of counts per second vs. spatial location along the line (Figure 14b). A considerable contrast is observed between the Pd 3d peak signal intensity obtained from the lifted-off Si (100) regions where Pd has grown easily and CF_x patterns which blocked Pd nucleation effectively, confirmed with a signal intensity equal to the noise floor of the XPS system. The EDX line-scan (Figure 14c) reveals that the intensity of Pd L X-ray quanta increases only within the non-CF_x coated line features which reaffirm the successful self-aligned deposition of Pd via polymerized fluorocarbon growth inhibitors.

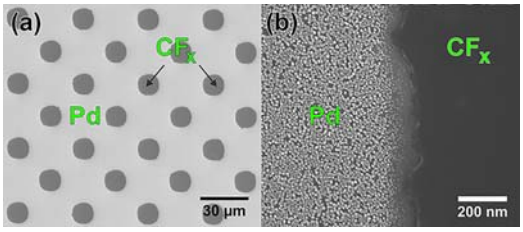

Figure 13. SEM and HR-SEM images of the patterned CF_x/Si sample surface after 2000 cycles of Pd-ALD. (a) SEM image showing the contrast of Pd-coated Si (100) and uncoated CF_x regions. (b) HR-SEM image of the Pd/CF_x interface which demonstrates the absence of Pd nucleation on ICP-polymerized CF_x blocking layer.

Figure 15 represents the EDX elemental mapping analyses of palladium, carbon, and fluorine elements at specific patterned areas after the 2000-cycle ALD experiment. Figure 15a corresponds to the SEM image of the patterned Pd line features through which elemental maps of Pd, C, and F are collected. Figure 15b-d show elemental maps of C K, Pd L, and F K, respectively. It is evident from these elemental maps that Pd is only present in the line features which coincide with the very Pd lines covering the non-CF_x coated regions shown in Figure 15a. Overall, XPS, EDX line scan, and EDX elemental mapping cumulatively confirm the selective deposition of Pd using 2000-cycle ALD on lithographically patterned CF_x inhibitor layers.

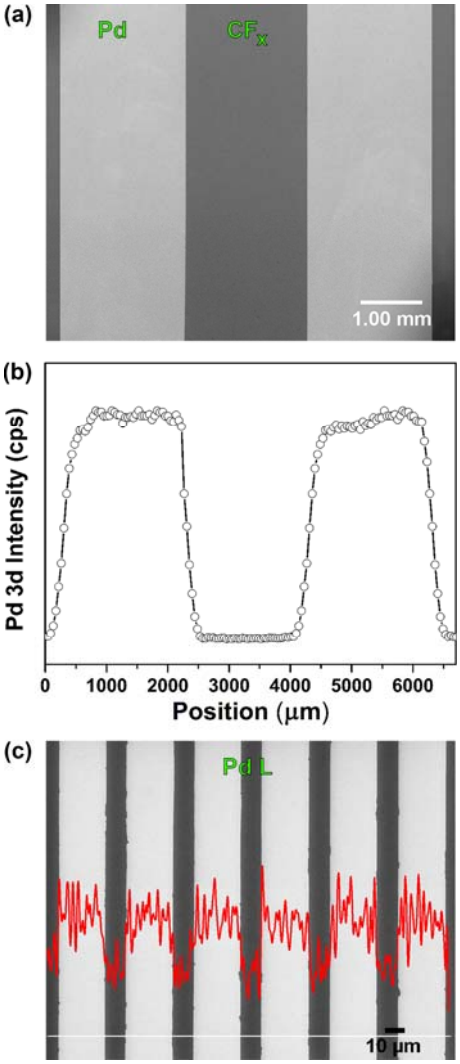

Figure 14. (a) SEM image and (b) XPS Pd 3d line scan obtained from Pd-ALD grown on mm-scale patterned CF_x/Si (100) sample. (c) EDX Pd L line scan superposed on the SEM image obtained from µm-scale CF_x/Si (100) patterned sample after 2000 Pd-ALD cycles.

In conclusion, we have presented a systematic investigation on the growth blocking/inhibition efficacy of plasma-polymerized CF_x layers to achieve selective deposition of Pt and Pd. We have demonstrated an effective yet relatively simple approach for low-temperature AS-ALD of Pt and Pd metal films on patterned CF_x/Si surfaces. The recorded nucleation delays for Pt and Pd correspond to equivalent blocking thicknesses of ~17 nm and ~10 nm, with the

selectivity ~0.99 both for Pt and Pd growth. This work confirms that plasma-polymerized CF_x layers effectively inhibit film growth not only for certain metal-oxides (ZnO) but for widely used noble metals (Pt, Pd) as well. The reason for CF_x blocking layer degrada-degradation during the ozone-based ALD process was concluded to be due to the oxygen physisorption with further hydroxyl groups formation on CF_x surface that creates the preferable centers for further Pt nucleation/growth. Our methodology can be utilized for various 3D device structures where selective Pt/Pd deposition on horizontal surfaces might be critically needed while blocking on other inclined and vertical surfaces. Moreover, the ozone-compatible selective deposition capability might pave the way for the AS-ALD of a wider set of materials which can benefit from ozone and alternative energetic co-reactants.

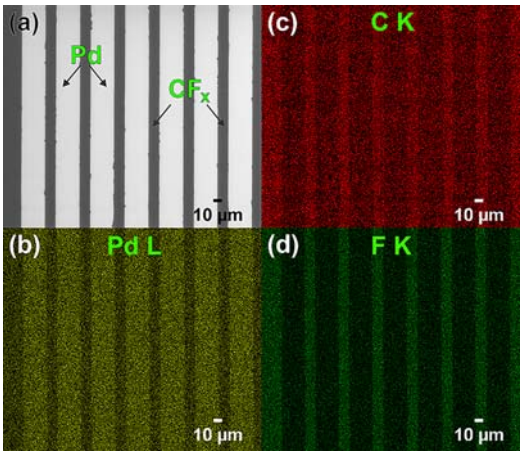

Figure 15. SEM image of (a) Pd/CF_x patterned sample after 2000-cycle Pd-ALD experiment. Elemental mapping of (b) Pd L, (c) C K, and (d) F K signals. Pd is colored in yellow, while red and green show C and F elements, respectively.

ASSOCIATED CONTENT

Supporting Information

This material is available free of charge via the Internet at http://pubs.acs.org

XPS survey scan; high-resolution XPS scans; variation in C, F at. % on CF_x/Si and C, Si at. % as a function of Pt ALD cycles; Pt binding energies on Si and on CF_x/Si; variation in C, F, O at. % on CF_x/Si and C, Si at. % on Si as a function of Pd ALD cycles; Pd binding energies.

AUTHOR INFORMATION

Corresponding Authors

*(N.B.) E-mail: necmi.biyikli@uconn.edu
*(P.D.) E-mail: p.deminskyi@gmail.com

Author Contributions

The manuscript was written through contributions of all authors. All authors have given approval to the final version of the manuscript.

Notes

The authors declare no competing financial interest.

ACKNOWLEDGMENT

The authors acknowledge (1) Institute of materials science and nanotechnology (UNAM), Bilkent University for the growth and material characterization facilities; (2) TUBITAK for their support under 2216 project for International Researcher.

REFERENCES

(1) Bent S. F. New strategies for area selective deposition. *ASD-2017*, 20–21 April, **2017**, Eindhoven, The Netherlands.

(2) Kim, W.-H.; Hashemi, F. S. M.; Mackus, A. J. M.; Bent, S. F. et al. A Process for Topographically Selective Deposition on 3D Nanostructures by Ion Implantation. *ACS Nano* **2016**, *10*, 4451–4458.

(3) Singh, J.; Thissen, N. F. W.; Kim, W. H.; Johnson, H.; Kessels, W. M. M.; Bol, A.; Bent, S. F.; Mackus, A. J. M. Area-selective Atomic Layer Deposition of Metal Oxides on Noble Metals Through Catalytic Oxygen Activation. *Chem. Mater*. **2018**, *30*, 663–670.

(4) Färm, E.; Kemell, M.; Ritala, M.; Leskelä, M. Selective-Area Atomic Layer Deposition with Microcontact Printed Self-Assembled Octadecyltrichlorosilane Monolayers as Mask Layers. *Thin Solid Films* **2008**, *517*, 972–975.

(5) Stevens, E.; Tomczak, Y.; Chan, B. T.; Sanchez, E. A.; Parsons, G. N.; Delabie, A. Growth Inhibition of TiN, TiO_2, and HfO_2 on Amorphous Carbon via Area-Selective Atomic Layer Deposition. *Chem. Mater*. **2018**, doi: 10.1021/acs.chemmater.8b00017.

(6) George, S. M. Atomic Layer Deposition: an Overview. *Chem. Rev.*, **2010**, *110*, 111–131.

(7) Leskela, M.; Ritala, M. Atomic Layer Deposition (ALD): From Precursors to Thin Film Structures. *Thin Solid Films* **2002**, *409*, 138–146.

(8) Serpell, C. J.; Cookson, J.; Ozkaya, D.; Beer, P. D. Core@shell Bimetallic Nanoparticle Synthesis via Anion Coordination. *Nat. Chem.* **2011**, *3*, 478−483.

(9) Mackus, A. J. M.; Kessels, W. M. M. et al. Room-Temperature Atomic Layer Deposition of Platinum. *Chem. Mater*. **2013**, *25*, 1769−1774.

(10) Hämäläinen, J.; Munnik, F.; Ritala, M.; Leskelä, M. Atomic Layer Deposition of Platinum Oxide and Metallic Platinum Thin Films from $Pt(acac)_2$ and Ozone. *Chem. Mater*. **2008**, *20*, 6840−6846.

(11) Knez, M.; Nielsch, K.; Niinisto, L. Synthesis and Surface Engineering of Complex Nanostructures by Atomic Layer Deposition. *Adv. Mater*. **2007**, *19*, 3425–3438.

(12) Groner, M. D.; Fabreguette, F. H.; Elam, J. W.; George, S. M. Low-Temperature Al_2O_3 Atomic Layer Deposition. *Chem. Mater*. **2004**, *16*, 639–645.

(13) Lim, B. S.; Rahtu, A.; Gordon, R. G., Atomic Layer Deposition of Transition Metals. *Nat. Mater*. **2003**, *2*, 749–754.

(14) Tang, J.; Cao, Q.; Han, S.-J. G. et al. Flexible CMOS Integrated Circuits Based on Carbon Nanotubes With sub-10 ns Stage Delays. *Nature Electronics* **2018**, *1*, 191–196.

(15) Mackus, A. J. M.; Bol, A. A.; Kessels, W. M. M. The Use of Atomic Layer Deposition in Advanced Nanopatterning. *Nanoscale*, **2014**, *6*, 10941–10960.

(16) Cao, K.; Cai, J.; Liu, X.; Chen, R. Review Article: Catalysts Design and Synthesis via Selective Atomic Layer Deposition. *J. Vac. Sci. Technol. A* **2018**, *36*, 010801(1)–010801(12)

(17) Seo, S.; Yeo, B. C.; Kim, H. et al. Reaction Mechanism of Area-Selective Atomic Layer Deposition for Al_2O_3 Nanopatterns. *ACS Appl. Mater. Interfaces* **2017**, *9*, 41607−41617.

(18) Mameli, A.; Mackus, A. J. M. et al. Area-Selective Atomic Layer Deposition of SiO_2 Using Acetylacetone as a Chemoselective Inhibitor in an ABC-Type Cycle. *ACS Nano* **2017**, *11*, 9303−9311.

(19) Ellinger, C. R.; Nelson, S. F. Selective Area Spatial Atomic Layer Deposition of ZnO, Al_2O_3, and Al-doped ZnO Using Poly(vinyl pyrrolidone). *Chem. Mater*. **2014**, *26*, 1514–1522.

(20) Junige, M. et al. Area-Selective Atomic Layer Deposition of Ru on Electron-Beam-Written Pt(C) Patterns Versus SiO_2 Substratum. *Nanotechnology* **2017**, *28*, 395301.

(21) Park, K. J.; Parsons, G. N. Selective Area Atomic Layer Deposition of Rhodium and Effective Work Function Characterization in Capacitor Structures. *Applied Physics Letters* **2006**, *89*, 043111.

(22) Jiang, X. R.; Huang, H.; Prinz, F. B.; Bent, S. F. Application of Atomic Layer Deposition of Platinum to Solid Oxide Fuel Cells. *Chem. Mater.* **2008**, *20*, 3897.

(23) Mackus, A. J. M.; Dielissen, S. A. F.; Mulders, J. J. L.; Kessels, W. M. M. Nanopatterning by direct-write atomic layer deposition. *Nanoscale* **2012**, *4*, 4477.

(24) Hong, J.; Porter, D. W.; Sreenivasan, R.; McIntyre, P. C.; Bent, S. F. ALD Resist Formed by Vapor-Deposited Self-Assembled Monolayers. *Langmuir* **2007**, *23*, 1160–1165.

(25) Park, M. H.; Jang, Y. J.; Sung-Suh, H. M.; Sung, M. M. Selective Atomic Layer Deposition of Titanium Oxide on Patterned Self-Assembled Monolayers Formed by Microcontact Printing. *Langmuir* **2004**, *20*, 2257–2260.

(26) Avila, J. R.; Demarco, E. J.; Emery, J. D.; Farha, O. K.; Pellin, M. J.; Hupp, J. T.; Martinson, A. B. F. Real-Time Observation of Atomic Layer Deposition Inhibition: Metal Oxide Growth on Self-Assembled Alkanethiols. *ACS Appl. Mater. Interfaces* **2014**, *6*, 11891–11898.

(27) Sadat, F.; Hashemi, M.; Birchansky, B. R.; Bent, S. F. Selective Deposition of Dielectrics: Limits and Advantages of Alkanethiol Blocking Agents on Metal–Dielectric Patterns. *ACS Appl. Mater. Interfaces*, **2016**, *8*, 33264–33272.

(28) Kim, J.-Y.; Kil, D.-S.; Kim, J.-H.; Park, S.-K. et al. Ru Films from Bis (ethylcyclopentadienyl) Ruthenium Using Ozone as a Reactant by Atomic Layer Deposition for Capacitor Electrodes. *Electrochem. Soc.* **2012**, *159*, H560.

(29) Hämäläinen, J.; Ritala, M.; Leskelä, M. Atomic Layer Deposition of Noble Metals and Their Oxides. *Chem. Mater.* **2014**, *26*, 786–801.

(30) Chen, Z.; Appenzeller, J.; Knoch, J.; Lin, Y.; Avouris, P. The Role of Metal-Nanotube Contact in the Performance of Carbon Nanotube Field-Effect Transistors. *Nano Lett.* **2005**, *5*, 1497−1502.

(31) Javey, A.; Guo, J.;Wang Q.; Lundstrom, M.; Dai, H. Ballistic Carbon Nanotube Field-Effect Transistors. *Nature* **2003**, *424*, 654–7.

(32) Luo, X.; Amine, K. et al. Pd Nanoparticles on ZnO-Passivated Porous Carbon by Atomic Layer Deposition: an Effective Electrochemical Catalyst For Li-O_2 Battery. *Nanotechnology* **2015,** *26*, 164003.

(33) Jiang, Y.; Chen, J.; Wang, R. et al. Ultralow Loading Palladium Nanocatalysts Prepared by Atomic Layer Deposition on Three-Dimensional Graphite-Coated Nickel Foam to Enhance the Ethanol Electro-Oxidation Reaction. *RSC Adv.*, **2016**, *6*, 13207–13216.

(34) Gu, D.; Baumgart, H.; Tapily, K.; Shrestha, P.; Namkoong, G.; Ao, X.; Müller, F. Precise Control of Highly Ordered Arrays of Nested Semiconductor/Metal Nanotubes. *Nano Res.* **2011**, *4*, 164−170.

(35) Kim, K.; Lee, H. B. R.; Bao, Z. Selective Metal Deposition at Graphene Line Defects by Atomic Layer Deposition. *Nat. Commun.* **2014**, *5*, 4781.

(36) Fleischmann, S.; Tolosa, A.; Zeiger, M.; Presser, V. et al. Vanadia–Titania Multilayer Nanodecoration of Carbon Onions via Atomic Layer Deposition for High-Performance Electrochemical Energy Storage. *J. Mater. Chem. A* **2017**, *5*, 2792–2801.

(37) Cao, K.; Zhu, Q.; Chen B. S. Controlled Synthesis of Pd/Pt Core-Shell Nanoparticles Using Area-selective Atomic Layer Deposition. *Sci. Rep.* **2015**, *5*, 8470.

(38) Mackus, A. J. M.; Mulders, J. J. L.; Sanden, M. C. M.; Kessels, W. M. M. Local Deposition of High-Purity Pt Nanostructures by Combining Electron Beam Induced Deposition and Atomic Layer Deposition. *J. Applied Physics* **2010**, *107*, 116102.

(39) Vervuurt, R. H. J.; Sharma, A.; Jiao, Y.; Kessels, W. M. M. Bol, A. A. Area-Selective Atomic Layer Deposition of Platinum Using Photosensitive Polyimide. *Nanotechnology* **2016**, *27*, 405302.

(40) Haider, A.; Deminskyi, P.; Khan, T. M.; Eren, H.; Biyikli N. Area-Selective Atomic Layer Deposition Using an Inductively Coupled Plasma Polymerized Fluorocarbon Layer: A Case Study for Metal Oxides. *J. Phys. Chem. C* **2016**, *120*, 26393–26401.

(41) Haider, A.; Yilmaz, M.; Deminskyi, P.; Eren, H.; Biyikli, N. Self-aligned atomic layer deposition of TiO_2 using tetrakis (dimethylamido)titanium on nanoscale patterned polymers. RSC Adv., **2016**, *6*, 106109.

(42) Peukert M. XPS investigation of surface oxidation layers on a platinum electrode in alkaline solution. *Electrochimica Acta.* **1984**, *29(10)*, 1315−1320.

(43) Nakamura, T.; Ichihara, S.; Den, T. Electrodeposition of FePt embedded into nanohole structures for magnetic recording media. *ECS Transactions*, **2007**, *3(25)*, 275−287.

(44) Wakisaka, M.; Suzuki, H.; Mitsui, S.; Uchida, H.; Watanabe, M. Increased Oxygen Coverage at Pt−Fe Alloy Cathode for the Enhanced Oxygen Reduction Reaction Studied by EC−XPS. J. Phys. Chem. C, 2008, 112, 7, 2750-2755.

(45) Bhushan, B.; Jung, Y. C. Wetting Study of Patterned Surfaces for Superhydrophobicity Ultramicroscopy. **2007**, *107*, 1033–1041.

(46) Hoshian, S.; Franssila, S. et al. Robust Superhydrophobic Silicon Without a Low Surface-Energy Hydrophobic Coating. *ACS Appl. Mater. Interfaces* **2015**, *7*, 941−949.

(47) Kelly, K. L.; Coronado, E.; Zhao, L. L.; Schatz, G. C. The Optical Properties of Metal Nanoparticles: The Influence of Size, Shape, and Dielectric Environment. *J. Phys. Chem. B* **2003**, *107*, 668.

(48) Astruc, D. Nanoparticles and Catalysis. *Wiley-VCH*: New York, **2008**.

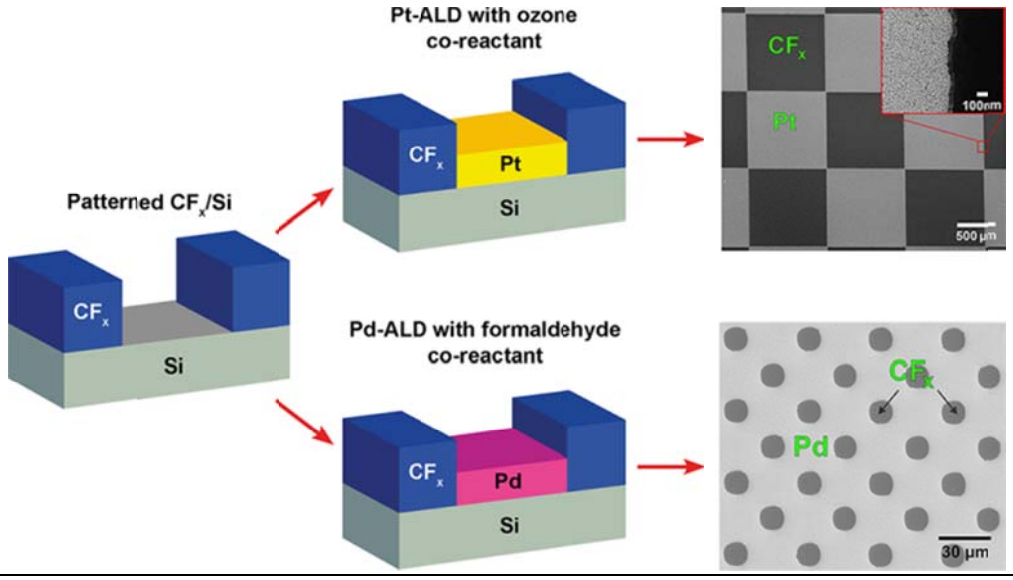
Pt-ALD with ozone
co-reactant
Patterned CFx/Si
CFx
Si
CFx
Pt
Si
CFx
Pt
100nm
500 µm
Pd-ALD with formaldehyde
co-reactant
CFx
Pd
Si
CFx
Pd
30 µm

Supporting information:

Area-selective atomic layer deposition of noble metals: polymerized fluorocarbon layers as effective growth inhibitors

Petro Deminskyi,[*,1,2] Ali Haider,[1] Hamit Eren,[3] Talha M. Khan,[1] and Necmi Biyikli[*,4]

[1] UNAM-Institute of Materials Science and Nanotechnology, Bilkent University, Ankara 06800, Turkey

[2] NASU-Institute of Microdevices, Technological & Analytical Research Department, Kiev 04136, Ukraine

[3] Department of Chemical Engineering, Delft University of Technology, van der Maasweg 9, 2629 HZ Delft, The Netherlands

[4] Electrical and Computer Engineering, University of Connecticut, 371 Fairfield Way, Storrs, CT, 06269-4157

*(N.B.) E-mail: necmi.biyikli@uconn.edu

*(P.D.) E-mail: p.deminskyi@gmail.com

Table S1. Variation in C, F at. % on CF_x/Si and C, Si at. % on Si surface as a function of Pt ALD cycles.

Number of ALD cycles	on CF_x/Si		on Si	
	C 1s, %	**F 1s**, %	**C 1s**, %	**Si 2p**, %
50	44.9	54.0	6.0	52.5
100	44.7	53.8	14.8	38.7
150	44.4	53.8	12.9	30.9
200	44.5	53.3	14.6	18.5
250	42.6	50.3	12.6	12.1

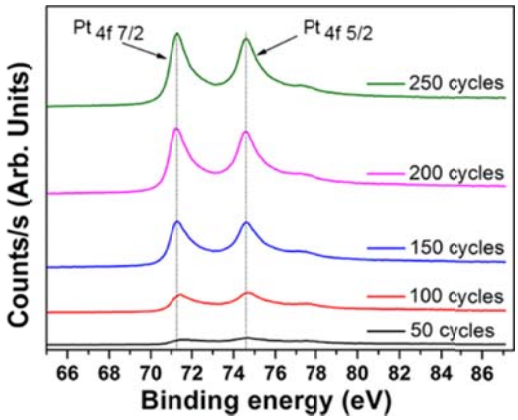

Figure S1. HR-XPS survey scans of Pt 4f obtained on Si(100) after 50, 100, 150, 200, and 250 Pt-ALD cycles.

A Pt 4f HR-XPS scans measured on Si samples taken after 50, 100, 150, 200, and 250 cycles of Pt-ALD (Figure S1 and Table S2) shows the general trend of intensification of Pt 4f peak: Pt $4f_{7/2}$ peak exhibits higher intensity than Pt $4f_{5/2}$ peak for Si(100) sample. In addition, for Si(100) reference samples, with increasing ALD cycles, a red-shift is observed in the Pt $4f_{7/2}$ and Pt $4f_{5/2}$ peaks, corresponding to core levels with lower binding energies. We attribute the presence of this red-shift, to the formation of Pt metal agglomerates and further quasi-continuous Pt metal thin film formation instead of PtO_x growth.[1] Indeed, the recorded $Pt4f_{5/2}$ and $Pt4f_{7/2}$ peaks for the initial 50 cycles (74.95 eV and 71.98 eV) and 100 cycles (74.96 eV and 71.68 eV) of Pt growth on Si(100) samples correspond to platinum (II) oxide (PtO) and platinum (IV)

oxide (PtO_2). After 150 cycles however, Pt $4f_{5/2}$ and Pt $4f_{7/2}$ peaks appeared at 74.6 eV and 71.28 eV, where the lower binding energy value is in good agreement with the reported values ranging from 70.6 eV to 71.3 eV for metallic Pt.[2,3] The higher binding energy, on the other hand, for 150 cycle Pt-ALD on Si(100) sample corresponds to the oxide state – PtO. We further confirmed the composition of as-synthesized Pt at 200 and 250 ALD cycles: Pt $4f_{5/2}$ peaks appeared at 74.6 eV and 74.54 eV, while Pt $4f_{7/2}$ peaks were observed at 71.19 eV and 71.26 eV for 200 and 250 cycles, respectively.

Table S2. The measured Pt binding energies of Pt, PtO, and PtO_2 sub-peaks on Si.

Number of ALD cycles	Pt binding energy (eV)	Spectral line	Element/ Compound	Reference
50	74.95 71.98	4f5/2 4f7/2	PtO_2 PtO	[4, 5]
100	74.96 71.68	4f5/2 4f7/2	PtO_2 Pt	[5, 6]
150	74.6 71.28	4f5/2 4f7/2	Pt-O Pt	[7, 8, 9]
200	74.6 71.19	4f5/2 4f7/2	Pt-O Pt	[7, 8, 9]
250	74.54 71.26	4f5/2 4f7/2	Pt-O Pt	[7, 8, 9]

Table S3. The measured binding energies of Pt, PtOH, Pt(IV)O sub-peaks on CF_x/Si samples as a function of ALD cycle number

Number of ALD cycles	Pt binding energy (eV)	Spectral line	Element/ Compound	Reference
50	-	-	-	-
100	-	-	-	-
150	-	-	-	-
200	75.40 78.56	4f5/2 4f7/2	Pt-OH Pt(IV)-O	[10, 11, 12]
250	74.91 78.29	4f5/2 4f7/2	Pt Pt(IV)-O	[6, 13, 14, 15]

Table S4. Variation in C, F, O at. % on CF_x/Si and C, Si at. % on Si as a function of Pd ALD cycles

Number of ALD cycles	**on CF_x/Si**			**on Si**		
	C 1s, %	**F 1s**, %	**O 1s** at. %	**C 1s**, %	**Si 2p**, %	**O 1s**, %
200	46.7	51.3	1.9	9.6	55.9	32.9
400	47.1	50.1	2.7	12.8	54.2	31.3
600	45.5	53.2	1.2	19.1	46.6	30.9
800	45.4	53.2	1.3	14.7	42.7	30.1
1000	45.6	52.6	1.7	18.6	44.5	32.5
1500	49.2	47.4	3.4	24.6	30.2	31.7
2000	49.6	47.3	2.9	24.2	30.5	36.8

Table S5. Binding energies of Pd, PdO, PdO_x on Si (100).

Number of ALD cycles	Pd binding energy (eV)	Spectral line	Element/ Compound	Reference
200	342.47 337.60 335.18	Pd $3d_{3/2}$ Pd $3d_{5/2}$ Pd $3d_{5/2}$	Pd-O PdO_x Pd	[16–18]
400	341.1 336.2 335.7	Pd $3d_{3/2}$ Pd $3d_{5/2}$ Pd $3d_{5/2}$	Pd PdO_x Pd	[17, 19, 20]
600	341.1 335.7	Pd $3d_{3/2}$ Pd $3d_{5/2}$	Pd	[19, 20]
800	340.5 335.42	Pd $3d_{3/2}$ Pd $3d_{5/2}$	Pd	[21, 22]
1000	340.5 335.2	Pd $3d_{3/2}$ Pd $3d_{5/2}$	Pd	[22, 23]
1500	340.3 335.19	Pd $3d_{3/2}$ Pd $3d_{5/2}$	Pd	[18, 24]
2000	340.3 335.1	Pd $3d_{3/2}$ Pd $3d_{5/2}$	Pd	[24]

REFERENCES

(1) Nist X-ray Photoelectron Spectroscopy Database, Version 4.1. *National Institute of Standards and Technology*, Gaithersburg, **2016**, http //srdata.nist.gov/xps/.

(2) Bhushan, B.; Jung, Y. C. Wetting Study of Patterned Surfaces for Superhydrophobicity Ultramicroscopy. **2007**, *107*, 1033–1041.

(3) Hoshian, S.; Franssila, S. et al. Robust Superhydrophobic Silicon Without a Low Surface-Energy Hydrophobic Coating. *ACS Appl. Mater. Interfaces* **2015**, *7*, 941−949.

(4) Zhai, L. et al. Fabrication of Graphene Aerogels with Heavily Loaded Metallic Nanoparticles. *Micromachines* **2017**, *8*, 47.

(5) Wang, X. et al. Electrocatalytic Activity and Interconnectivity of Pt Nanoparticles on Multiwalled Carbon Nanotubes for Fuel Cells. *J. Phys. Chem. C* **2009**, *113*, 18935–18945.

(6) Shukla, K. Durable Transition-Metal-Carbide-Supported Pt–Ru Anodes for Direct Methanol Fuel Cells. *J. Fuel Cells* **2012**, *12*, 146–152.

(7) Bhushan, B.; Jung, Y. C. Wetting Study of Patterned Surfaces for Superhydrophobicity. *Ultramicroscopy* **2007**, *107*, 1033–1041.

(8) Allen, G. C.; Tucker, P. M. X-Ray Photoelectron Spectroscopy of Adsorbed Oxygen and Carbonaceous Species on Platinum Electrodes. *Electroanalytical Chemistry and Interfacial Electrochemistry*, **1974**, *50*, 335743.

(9) Lin, Y. et al. Highly Uniform Distribution of Pt Nanoparticles on N-doped Hollow Carbon Spheres with Enhanced Durability for Oxygen Reduction Reaction *RSC Adv.* **2017**, *7*, 6303–6308.

(10) Shi, D. et al. An advanced Electrocatalyst with Exceptional Eletrocatalytic Activity via Ultrafine Pt-Based Trimetallic Nanoparticles on Pristine Graphene. *J. Carbon* **2015**, *87*, 116–127.

(11) Frelink, T.; Visscher W.; Cox A. P. Ellipsometry and Dems Study of the Electrooxidation of Methanol at Pt and Ru and Sn-promoted Pt. *J. Electrochim Acta* **1995**, *40*, 1537–43.

(12) Chen, S. et al. One-pot Synthesis of Graphene/Carbon Nanospheres/Graphene Sandwich Supported Pt_3Ni Nanoparticles with Enhanced Electrocatalytic Activity in Methanol Oxidation. *International journal of hydrogen energy* **2015**, *40*, 5106–5114.

(13) Guha, A. et al. Surface-Modified Carbons as Platinum Catalyst Support for PEM Fuel Cells *J. Carbon* **2007**, *45*, 1506–1517.

(14) Wang, X.; Hsing, I. M. Surfactant Stabilized Pt and Pt Alloy Electrocatalyst for Polymer Electrolyte Fuel Cells. *J. Electrochim Acta* **2002**, 47, 2981–7.

(15) Mondal A.; Jana N. R. Effect of Size and Oxidation State of Platinum Nanoparticles on the Electrocatalytic Performance of Graphene-Nanoparticle Composites. *RSC Adv.* **2015**, *5*, 85196–85201.

(16) Militello, M. C.; Simko, S. J. Palladium Oxide (PdO) by XPS. *Surf. Sci. Spectra* **1994**, *3*, 395.

(17) Tura, J. M.; Regull, P.; Victori, L.; Castellar, D. XPS and IR (ATR) Analysis of Pd Oxide Films Obtained by Electrochemical Methods. *Surf. Interface Anal.* **1988**, *11*, 447.

(18) Bird R. J.; Swift P. Energy Calibration in Electron Spectroscopy and the re-Determination of Some Reference Electron Binding Energies. *J. Electron Spectrosc. Relat. Phenom.* **1980**, *21*, 227.

(19) Tressaud, A.; Khairoun, S.; Touhara, H.; Watanabe, N. X-Ray Photoelectron Spectroscopy of Palladium Fluorides *J. Z. Anorg. Allg. Chem.* **1986**, *540*, 291.

(20) Bertolini, J. C.; Delichere, P.; Khanra, B. C.; Massardier, J.; Noupa, C.; Tardy, B. Electronic Properties of Supported Pd Aggregates in Relation with Their Reactivity for 1,3-Butadiene Hydrogenation. *Catal. Lett*. **1990**, *6*, 215.
(21) Militello, M. C.; Simko, S. J. Elemental Palladium by XPS *Surf. Sci. Spectra* **1994**, *3*, 387.
(22) Pulm, H.; Hohlneicher, G.; Freund, H. J. J. Less-common Metals *NIST XPS Database Scientific Citation Search Result* **1986**, *115*, 127.
(23) Hedman, J. Klasson, M.; Zyranov, V. G. et al. The Electronic Structure of Some Palladium Alloys Studied by ESCA and X-ray Spectroscopy. *Phys. Scripta,* **1971**, *4*, 195.
(24) Jenks, C. J.; Chang, S. L.; Anderegg, J. W.; Thiel, P. A.; Lynch, D. W. Photoelectron Spectra of an $Al_{70}Pd_{21}Mn_9$ Quasicrystal and the Cubic Alloy $Al_{60}Pd_{25}Mn_{15}$. *Phys. Rev. B* **1996**, *54*, 6301.